processes

Article

Analysis of Laser Cutting Process for Different Diagonal Material Shapes

Jungsoo Choi, Ryoonhan Kim, Danbi Song, Dae-Won Cho *, Jeong Suh, Seonmin Kim and Sang-Hyun Ahn

Busan Machinery Research Center, Korea Institute of Machinery and Materials, Busan 46744, Republic of Korea
* Correspondence: dwcho@kimm.re.kr

Abstract: In this study, the laser cutting characteristics were analyzed according to the shape of the back side of the specimen, and the laser cutting characteristics were compared according to the thickness of the edge (10 mm, 20 mm, and 30 mm). A Yb-YAG laser was used in this study, and the cutting target was STS304 with a thickness of 50 mm, and the cutting process was analyzed using a high-speed camera. In the experiment, it was found through image analysis that the cutting performance was excellent at 30 mm thickness of the edge. In order to analyze this reason, a thermal conduction analysis (numerical simulation) was performed, and it was confirmed that the thicker thickness of the edge caused a preheating effect during laser cutting due to a large amount of heat accumulation. This effect can be used as a reference for the initial processing state while cutting thick metals as it is a characteristic that has not been revealed before.

Keywords: conductive heat transfer; diagonal shape; high-speed camera; laser cutting; laser processing; numerical simulation; Yb-YAG laser

Citation: Choi, J.; Kim, R.; Song, D.; Cho, D.-W.; Suh, J.; Kim, S.; Ahn, S.-H. Analysis of Laser Cutting Process for Different Diagonal Material Shapes. *Processes* **2022**, *10*, 2743. https://doi.org/10.3390/pr10122743

Academic Editor: Antonino Recca

Received: 2 December 2022
Accepted: 15 December 2022
Published: 19 December 2022

1. Introduction

In recent years, research on the maximum cutting thickness and maximum feed rate of laser cutting has increased significantly because laser power increases with the development of laser sources [1]. Laser cutting has begun to play a significant role in industries owing to several advantages, including fast production speed, excellent cutting quality, and no tool abrasion. They can even be used in automobiles, aerospace, shipbuilding, and material manufacturing businesses and for cutting composite materials such as metals, plastics, cement, and ceramics [2–7].

A representative example of non-metal cutting is carbon-fiber-reinforced polymers (CFRP) cutting. CFRPs are not suitable for mechanical cutting methods, such as drilling and milling, applied to metal parts for processing composite materials. This is because the high strength of CFRP causes severe wear. However, laser cutting is a non-contact non-grinding process that is suitable for replacing existing mechanical cutting methods [8].

Laser cutting is also used to cut dental materials that require delicate processing, such as ceramics and resins. Since laser cutting, which is a non-contact method, does not require a blade, the contamination of the material is reduced. Additionally, unlike mechanical cutting, a laser beam is not worn [9]. It is also used in thermoplastic materials, such as poly methyl methacrylate (PMMA) in sensors, smartphones, and car windows. In addition, it is gaining attention as an important technology for processing and cutting electric cars and portable electric equipment. The use of laser cutting in standardized and automated locations has high initial investment costs. However, it leads to long-term cost savings in terms of maintenance [10].

The recent development of high-power lasers has enabled the laser cutting of metals in many industries, such as for cutting plates of thickness ranging from 10 mm or less to 100 mm. In the case of metal equipment processing of less than 10 mm, laser processing has the advantage of being able to perform welding immediately without secondary processing because the quality of the cut surface is superior to that of plasma and flame processing. When the thickness of the object is 10 mm or greater, the formation of secondary contaminants is insignificant because the kerf width is relatively narrow. The key to laser cutting is to concentrate heat by focusing a beam spot on a small area. When a beam is focused, the high-temperature beam melts, evaporates, and blows the molten material with the assistant gas. Therefore, in laser cutting, it is important to select the optimal assistant gas and flow rate by considering the melt characteristics caused by the heat input of the laser beam [11].

The assistant gas plays an important role in laser cutting. The assistant gas transmitted through the nozzle significantly influences the removal of the molten material of the specimen melted by the laser beam. The gas shape formed at the nozzle outlet affects the cutting thickness and surface roughness. Therefore, the appropriate design of a nozzle is important for improving the cutting quality [12–15]. Since the gas flow depends on the nozzle diameter and distance between the nozzle and the cutting target, it becomes a variable in the cutting process [16,17]. A high assistant gas flow rate does not necessarily mean that the cutting quality is good, and it is important to have an optimized nozzle design [18]. The cutting surface roughness is also caused by auxiliary gas flow, and the smaller the shape in which the cutting surface is changed, the better the cutting quality. When the cutting surface changes, the roughness of the lower part increases rapidly, making it difficult to remove the dross [19,20]. Additionally, a decrease in the slope of the top and bottom surfaces of the cut plane reduces the occurrence of shock wave structures [17,21]. Gas flow images are captured using a high-speed camera for understanding the assisting gas flow. In this experiment, the behavior of the cutting molten pool was photographed using a high-speed camera [22,23].

In a study conducted by Tamura et al. [5] for cutting objects in various environments, STS304 material of thickness up to 200 mm was cut obliquely using a specimen of SM490A material. The output power was 30 kW, and as the specimen was cut at 37° at a rate of 20 mm/min, the stand-off distance varied from 125–88 mm.

Fushimi et al. conducted an experiment in which the assistant gas was ejected to minimize dross by separately disposing of the laser-cutting gas at the bottom and not coaxial with the laser. The slope of the lower end of the sample was set to 45°, and the experiment was conducted to cut through one pipe or to reduce the dross through two assistant gas pipes [11].

Similarly, a study was conducted to increase the efficiency by using assistant gas at the bottom or cutting the specimen obliquely to reduce the dross of the specimen. However, there have been no studies related to the shape of the specimen, and it is necessary to understand how the performance of metal cutting changes according to the shape of the specimen. Moreover, an efficient method for cutting thick objects using a relatively low output needs to be investigated. For this, experiments were conducted using specimens with various thickness changes, and thermal conduction simulation was performed to identify the cause of cutting. It is believed that laser cutting can be made more efficient by using thermal conduction. Based on this research, it is expected to be used as a reference when cutting thick metal.

2. Experimental Procedure

An experiment was conducted to determine the effect of thermal accumulation during laser cutting as the volume of the specimen increased. STS304 was the experimental specimen used, and its composition is listed in Table 1.

Table 1. Mill test certificate (%).

	Fe	C	Si	Mn	P	S	Cr	Ni	Mo	N	Co	Cu
composition	71.636	0.016	0.37	1.50	0.021	0.003	18.24	8.12	0.01	0.044	0.03	0.01

As a condition for this experiment, a Yb:YAG disk laser was used with a laser focusing focal length of 300 mm, NA specification of 99.5%, and a laser wavelength of 1030 nm. The cutting nozzle was 3 mm in diameter and the gap between the material and the cutting nozzle was 1 mm. The output power was 8 kW, and nitrogen gas was used at 10 bar and a constant speed of 2.9 mm/s. The thickness of the specimen shape width was 50 mm, with four shape variables, as shown in Figure 1 and Table 2.

Table 2. Specimen shapes.

Case	L1 (mm)	L2 (mm)	D1 (mm)	D2 (mm)	D3 (mm)	Cutting Speed (mm/s)
Case1	50	50	100	100	1	2.3
Case2	10	50	100	60	1	2.9
Case3	20	50	100	60	1	2.9
Case4	30	50	100	60	1	2.9

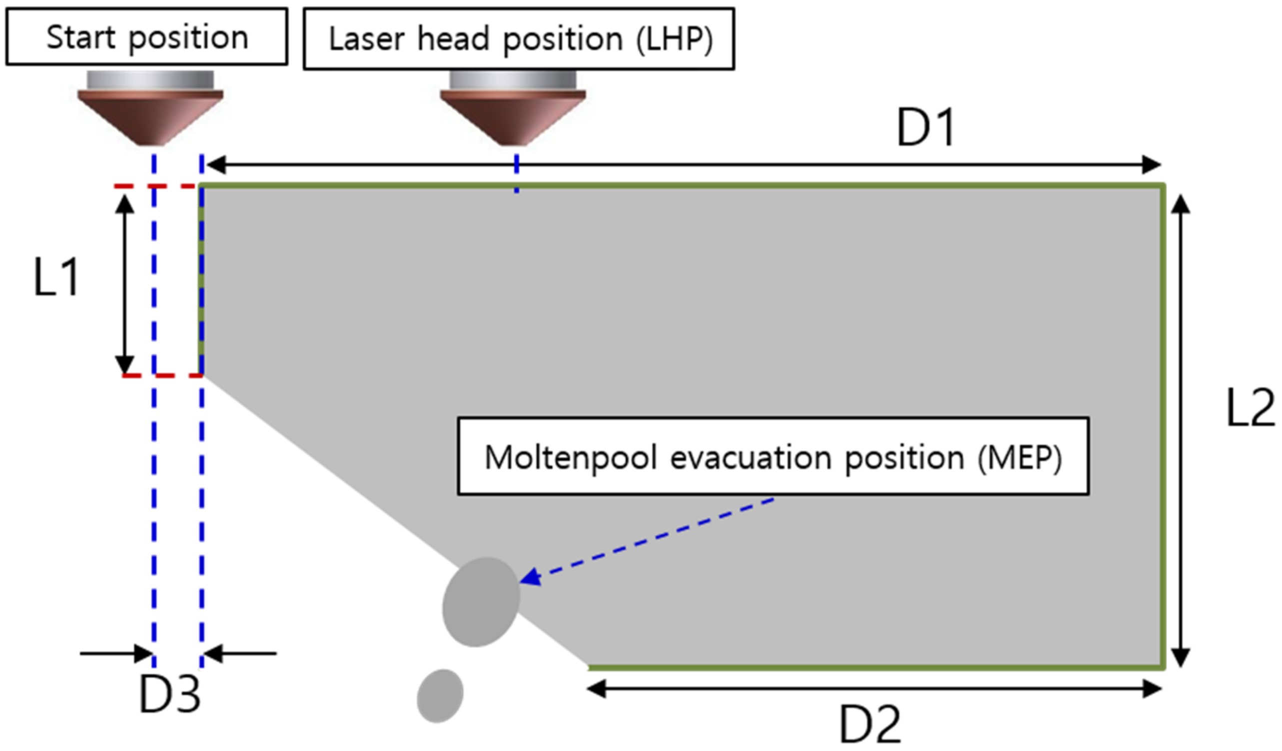

Figure 1. Specimen shapes.

The laser equipment and jig were set as shown in Figure 2.

The experiment was conducted after the specimens were fixed. A Photron FASTCAM SA4 high-speed camera was installed to observe the shape of laser cutting. A band-pass filter was used to observe the molten pool during the photography. The shutter speed was 1/2000 s, and the frame per second (FPS) was 250.

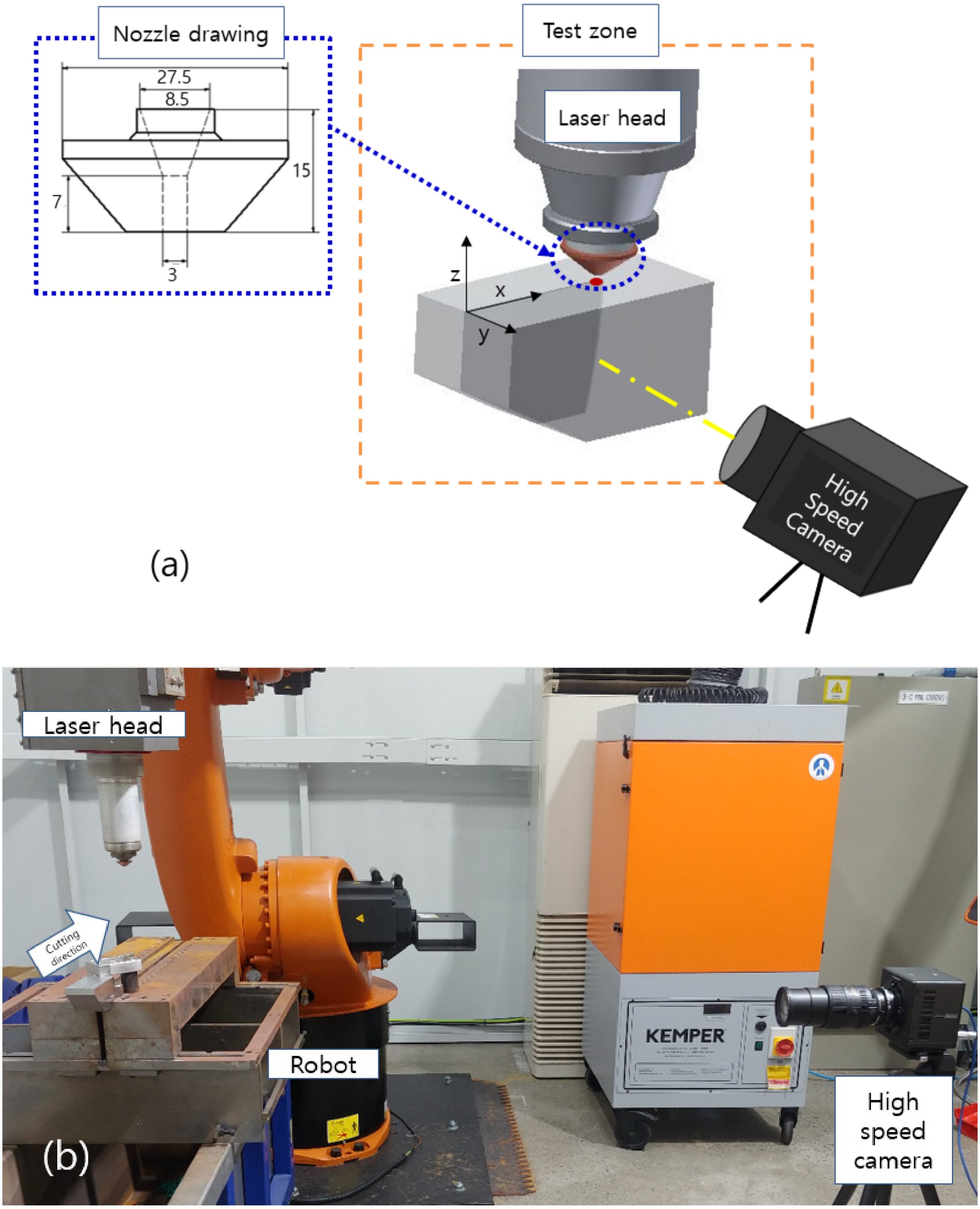

Figure 2. Experimental setup: (**a**) Schematic and (**b**) laser cutting experimental set-up.

3. Results and Discussion

Figure 3 shows the images of different cutting conditions. The upper cutting lengths were (a) 22 mm, (b) 59 mm, and (c) and (d) 70 mm.

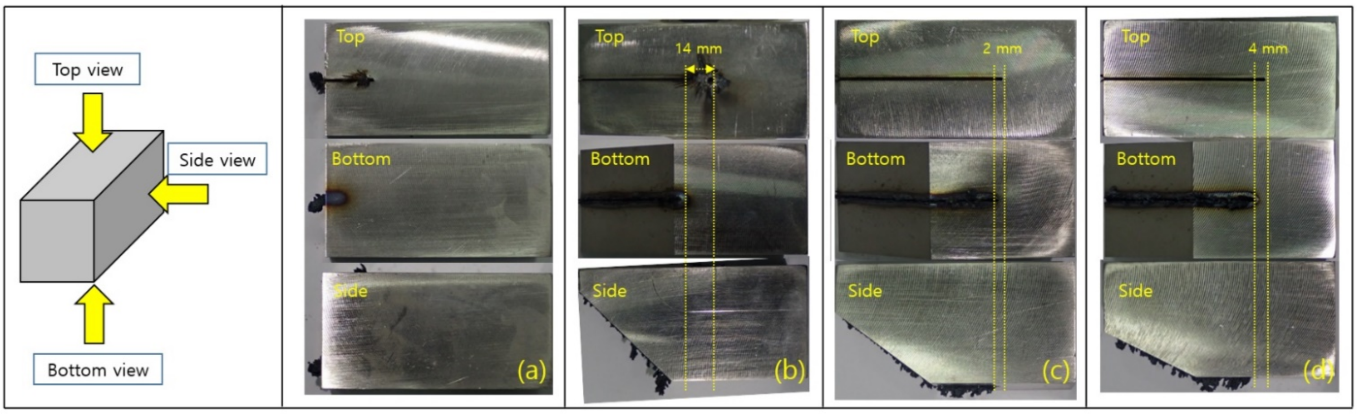

Figure 3. Cut specimen images: (**a**) case 1, (**b**) case 2, (**c**) case 3, and (**d**) case 4.

The cross-section of case 2 in Figure 4d shows that the cutting melt was not evacuated to the bottom and side. Hence, it was evacuated to the top. This phenomenon is believed to have occurred because the laser light energy did not sufficiently melt the specimen Therefore, it melted and then solidified to obstruct the gas flow. This phenomenon was not observed in Figure 4b case 3 and Figure 4c case 4, where amputation was performed.

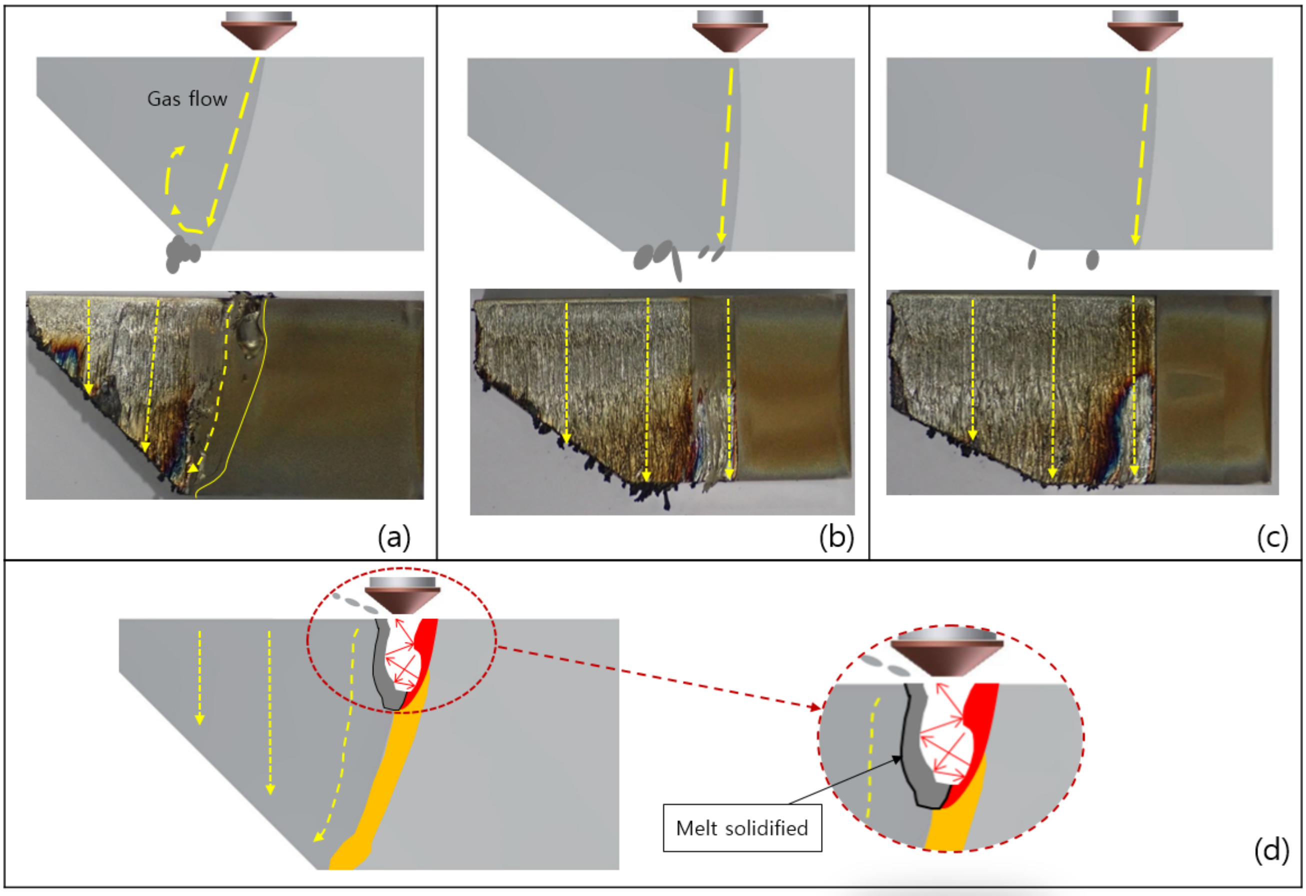

Figure 4. Longitudinal cross section of cut specimen: (**a**) case 2, (**b**) case 3, and (**c**) case 4. (**d**) Schematic of case 2 cause analysis.

The specimen of case 1 failed to cut at a speed of 2.3 mm/s. The dross was not evacuated from the bottom in the initial part of the experiment, as shown in Figure 5a; however, it was evacuated from the side direction. The melt that was evacuated from the side direction accumulated and solidified. Although the laser head advanced, it did not evacuate to the bottom of the dross. It is possible to observe the shape in which the melt flows back and rises upward at the laser head position (LHP), as shown in Figure 5e,f. Therefore, the experiment was stopped because it was considered to be a cutting failure.

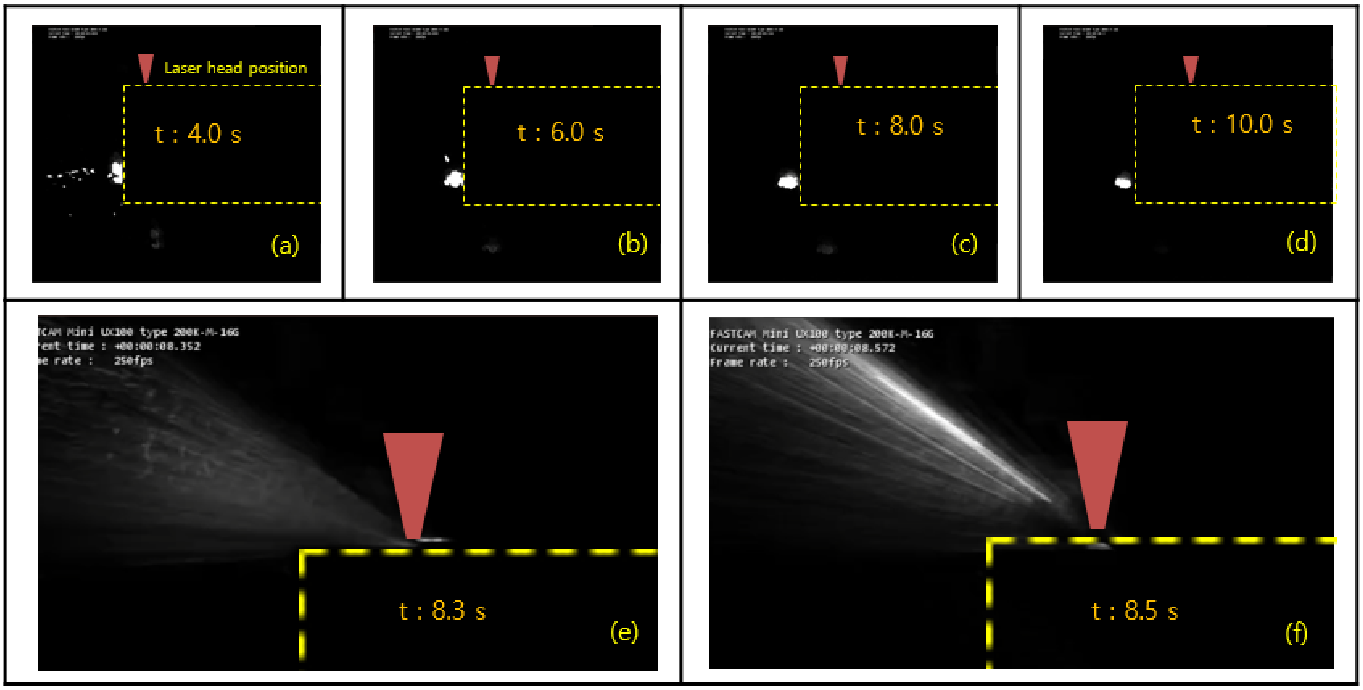

Figure 5. Molten pool behavior and evacuation captured by the high-speed camera in case 1 at (**a**) t: 4.0 s, (**b**) t: 6.0 s, (**c**) t: 8.0 s, (**d**) t: 10.0 s, (**e**) t: 8.3 s, and (**f**) t: 8.5 s.

Among the four experiments, case 2 was cut, as shown in Figure 6. The upper part of the image is the LHP, and the bottom part is the molten pool evacuation position (MEP). In the case where the position of the LHP and dross from the bottom were similar, the melt discharge was emitted in the downward direction for 1–16 s, as shown in the image. However, the difference in the dross position from the LHP and the bottom section (in Figure 6i), which is the moment when the melt accumulates and solidifies on the side, was observed, and the melt could not be discharged to the bottom. Finally, the difference in cutting length between the upper and lower parts was 14 mm.

Figure 6i,j show that as the molten pool hardened, its color turned grey. As shown in Figure 6k, after 20 s, a phenomenon in which the melt cannot evacuate to the bottom and the melt rises to the top was observed at Figure 6m.

Case 3 was cut, as shown in Figure 7. A small difference between the LHP and molten pool evaporation positions from the bottom was observed, and the melt was discharged smoothly. Finally, the difference between the cutting positions indicated on the lower end of Figure 7l at the end time and LHP resulted in a distance difference of 2 mm.

Similar to case 3, the LHP and MEP of the entire cutting section in case 4 were similar. Figure 8l shows the end of the cutting, and the dross cooling and hardening. Finally, the difference between the cut position of the lower end in Figure 8l and the position of the LHP at the endpoint was 4 mm.

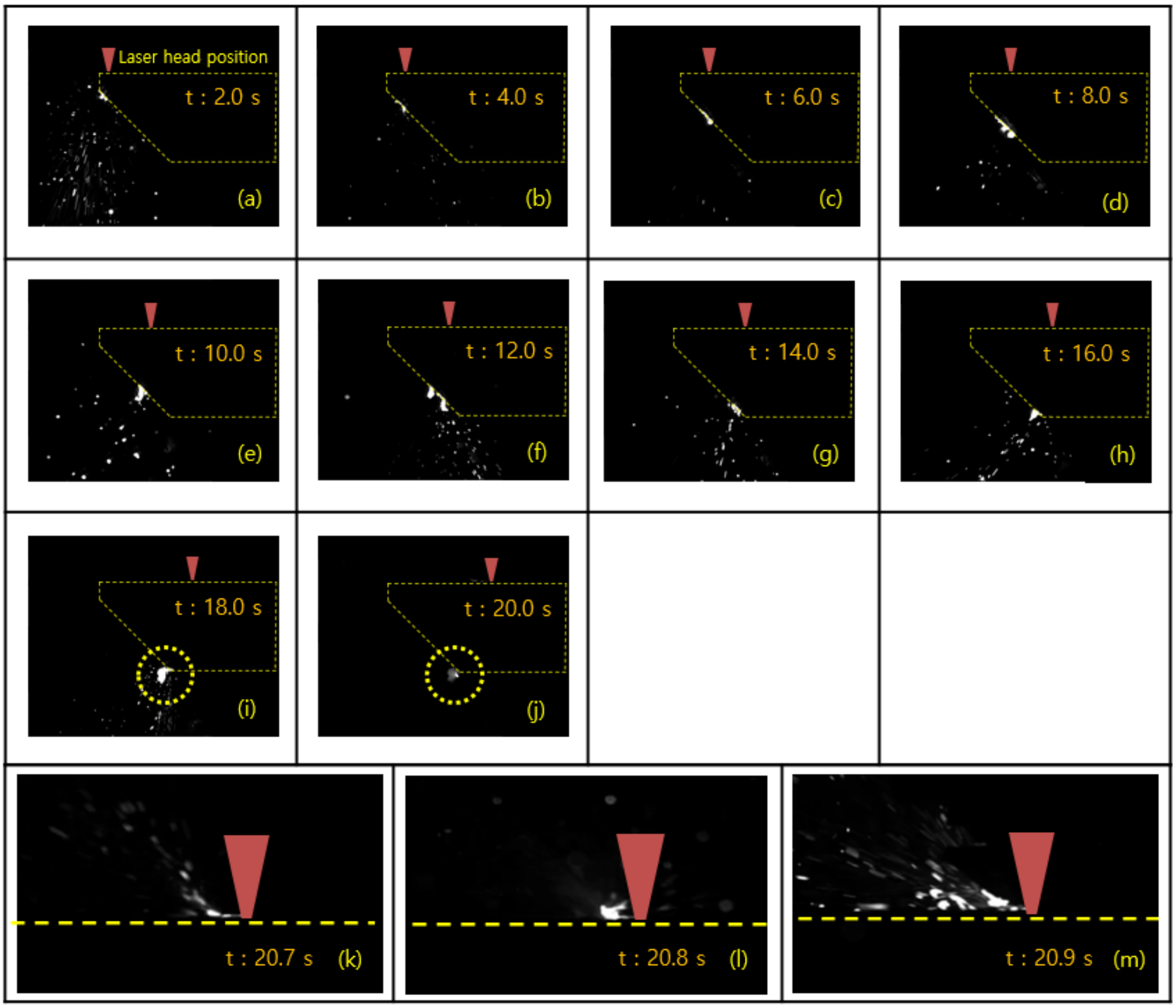

Figure 6. Molten pool behavior and evacuation captured by the high-speed camera in case 2 at (**a**) t: 2.0 s, (**b**) t: 4.0 s, (**c**) t: 6.0 s, (**d**) t: 8.0 s, (**e**) t: 10.0 s, (**f**) t: 12.0 s, (**g**) t: 14.0 s, (**h**) t: 16.0 s, (**i**) t: 18.0 s, (**j**) t: 20.0 s, (**k**) t: 20.7 s, (**l**) t: 20.8 s, and (**m**) t: 20.9 s.

Proceeding from case 2 to case 4, the MEP is shown in Figure 9. Within 17 s of the start of cutting in the three cases, the positions of the LHP and MEP were similar. However, after 17 s, the MEP in case 2 remained constant, while the LHP increased.

In this study, we focus on the physical effects of these differences. Figure 10 shows the results of the thermal conduction analysis for 10 s, assuming that the temperature of the cut front is 1800 K and the kerf wall temperature, as the initial boundary condition of the thermal conduction analysis, is 1200 K. The initial temperature of the material was set to 298 K, and a plane symmetry boundary was applied for analysis efficiency. In particular, the initial temperature condition of the cut front assumes that the kerf wall is mostly near the melting temperature when the laser is melted and blown out by the gas. The model used in this study is energy conservation and is expressed as Equation (1) [24,25].

$$\frac{\partial(\rho CT)}{\partial t} = \frac{\partial^2(kT)}{\partial x^2} + \frac{\partial^2(kT)}{\partial y^2} + \frac{\partial^2(kT)}{\partial z^2} \tag{1}$$

where ρ, C, and k refer to the density of STS304, specific heat, and thermal conductivity, respectively.

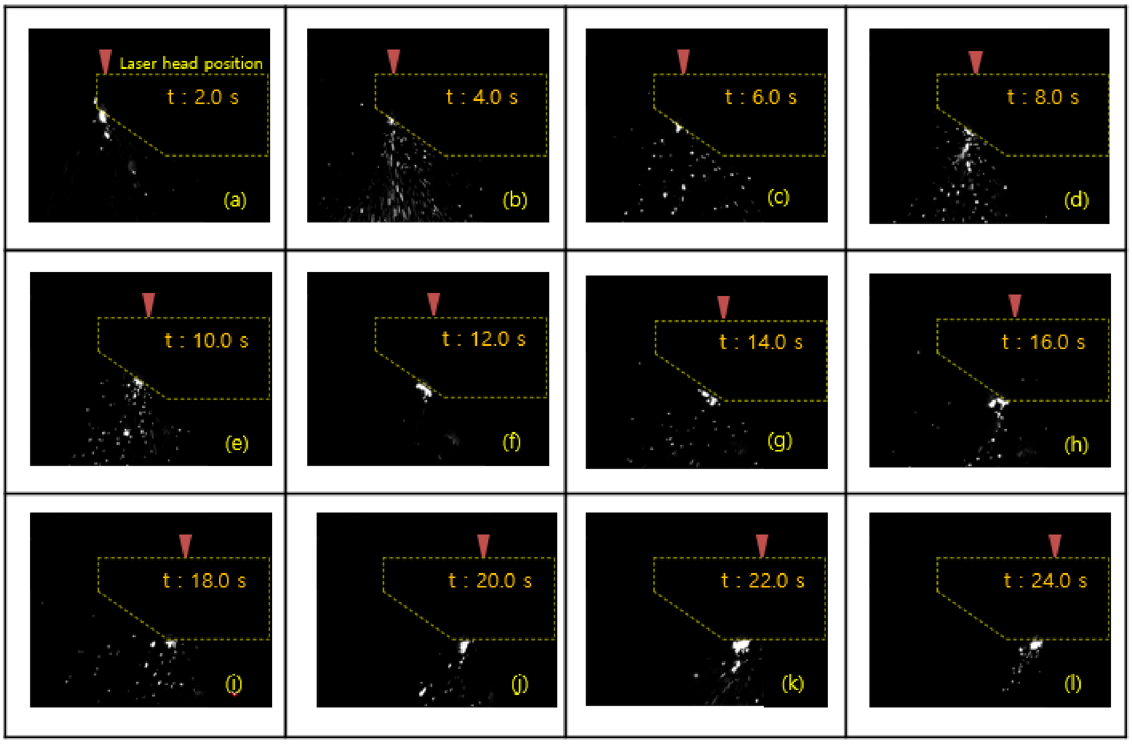

Figure 7. Molten pool behavior and evacuation captured by the high-speed camera in case 3 at (**a**) t: 2.0 s, (**b**) t: 4.0 s, (**c**) t: 6.0 s, (**d**) t: 8.0 s, (**e**) t: 10.0 s, (**f**) t: 12.0 s, (**g**) t: 14.0 s, (**h**) t: 16.0 s, (**i**) t: 18.0 s, (**j**) t: 20.0 s, (**k**) t: 22.0 s, and (**l**) 24.0 s.

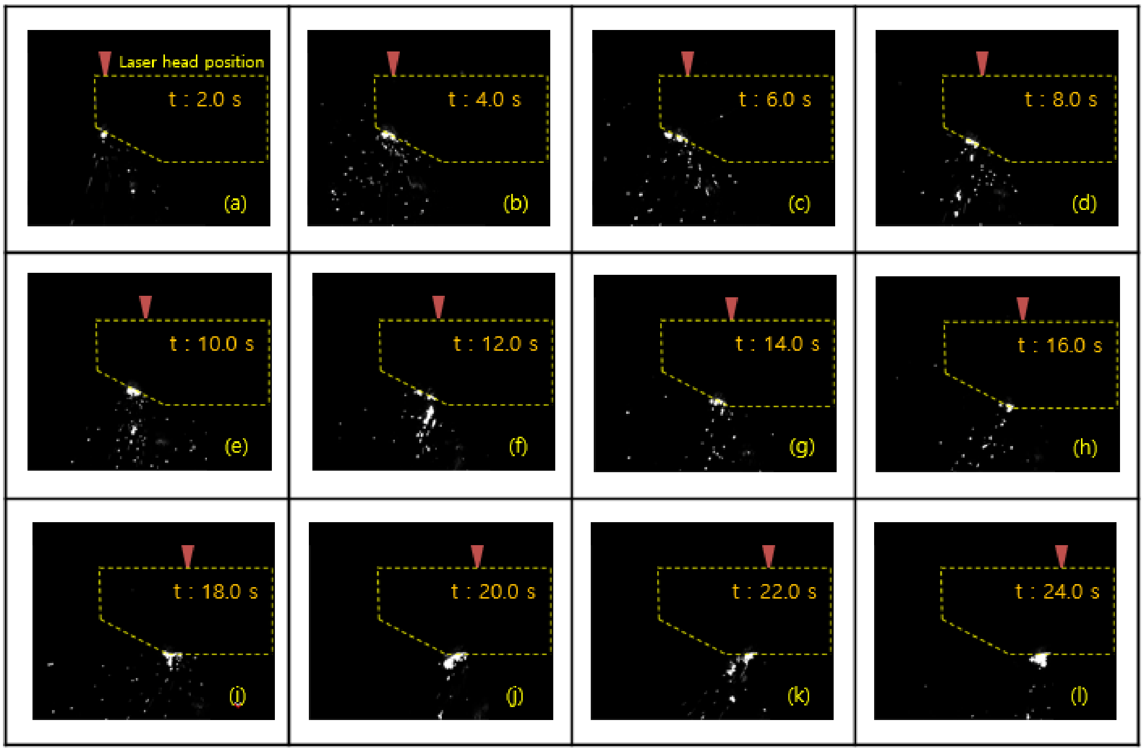

Figure 8. Molten pool behavior and evacuation captured by the high-speed camera in case 4 at (**a**) t: 2.0 s, (**b**) t: 4.0 s, (**c**) t: 6.0 s, (**d**) t: 8.0 s, (**e**) t: 10.0 s, (**f**) t: 12.0 s, (**g**) t: 14.0 s, (**h**) t: 16.0 s, (**i**) t: 18.0 s, (**j**) t: 20.0 s, (**k**) t: 22.0 s, and (**l**) t: 24.0 s.

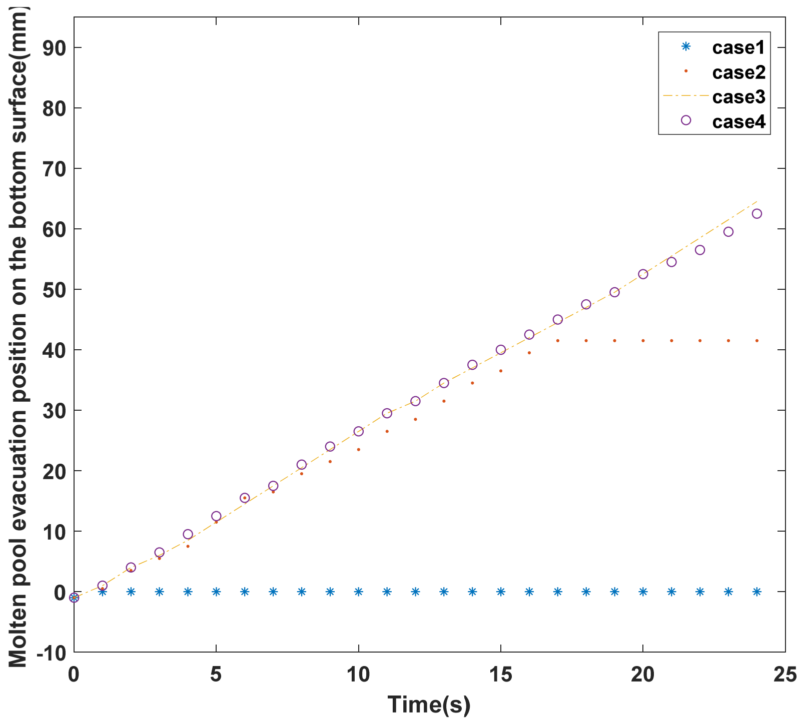

Figure 9. Location of molten pool evacuation on the bottom surface along the x-direction for a variable time.

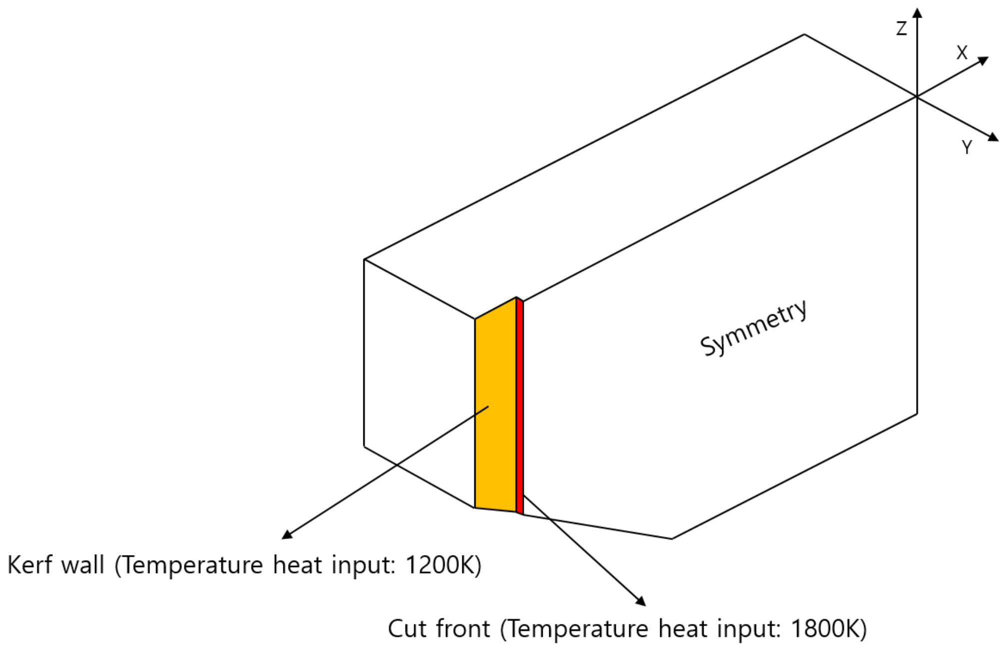

Figure 10. Boundary condition of simulation (symmetry).

Figure 11 shows the simulated 3D thermal cutting results using the specimen shapes in cases 2 and 4. Therefore, it expresses the thermal conduction result for the case in which the shape of the specimen is different. A comparison of local temperature changes was drawn for a more detailed analysis, as shown in Figures 12–14.

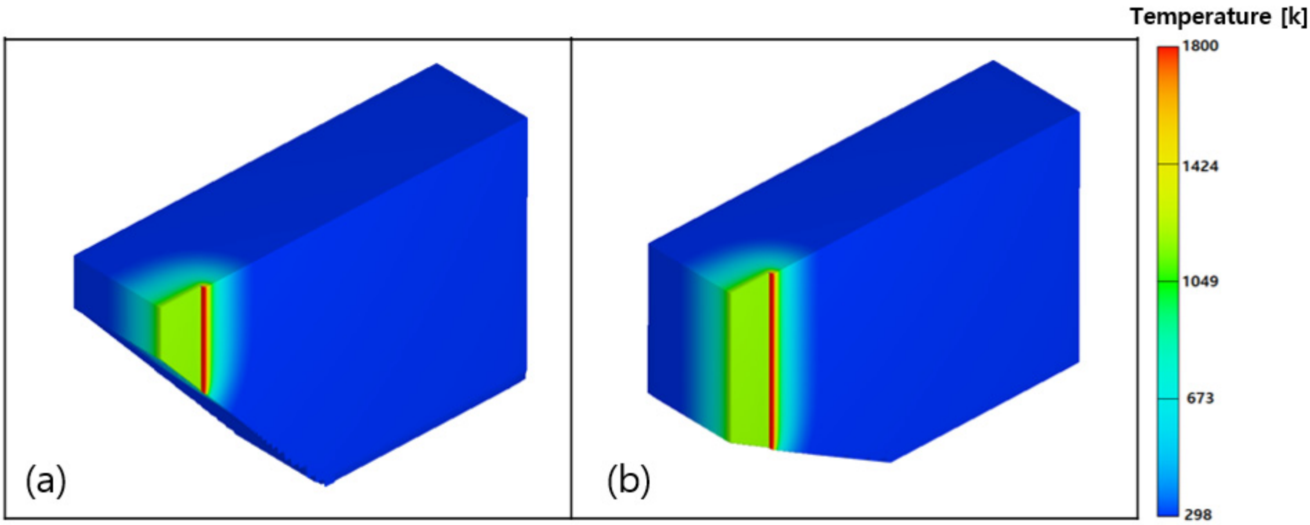

Figure 11. Numerical simulation of heat conduction for different cases: (**a**) half scale of case 2 and (**b**) half scale of case 4.

Figure 12 shows the temperatures for the symmetry plane. The overall temperature trend is similar. However, the shape of the isotherm for the bottom surface is different. For a more detailed analysis of these results, the temperature distribution for the region is expressed locally in Figure 13. Each isotherm is distributed almost perpendicular to the slope. Therefore, the distribution of these isotherms is very different in cases 2 and 4 due to the size of pre-heating effect, and the temperature graph for each location on the white dotted line in Figure 13a,b can be expressed as shown in Figure 14.

Figure 14 shows the temperatures in the x-direction, and the temperature of case 4 is observed to be at most 200 °C higher than that of case 2. Therefore, in case 4, where the edge is thick, more efficient thermal conduction occurs from the bottom diagonal surface, indicating that it can be maintained at a relatively high temperature. These mechanisms are shown in Figures 15 and 16, respectively. Assuming that the same temperature for cases 2 and 4 are applied, the thicker cut front (case 4) can bring a greater amount of heat energy in the x-direction. In case 2, the thickness of the slope increases rapidly, and the temperature rises slowly. On the other hand, the slope starts with a thick thickness at the edge start point and the slope thickness increases smoothly in case 4. Therefore, since there is a lot of heat transfer according to heat conduction in case 4, the greater preheating effect can be observed. Thus, if the cutting is successful by edge-start cutting at the initial stage, the material with a relatively thicker edge material can bring a larger amount of heat accumulation in the laser cutting process. The accumulated heat induces a temperature increase effect in the direction of cutting progress, and relatively more efficient cutting is performed.

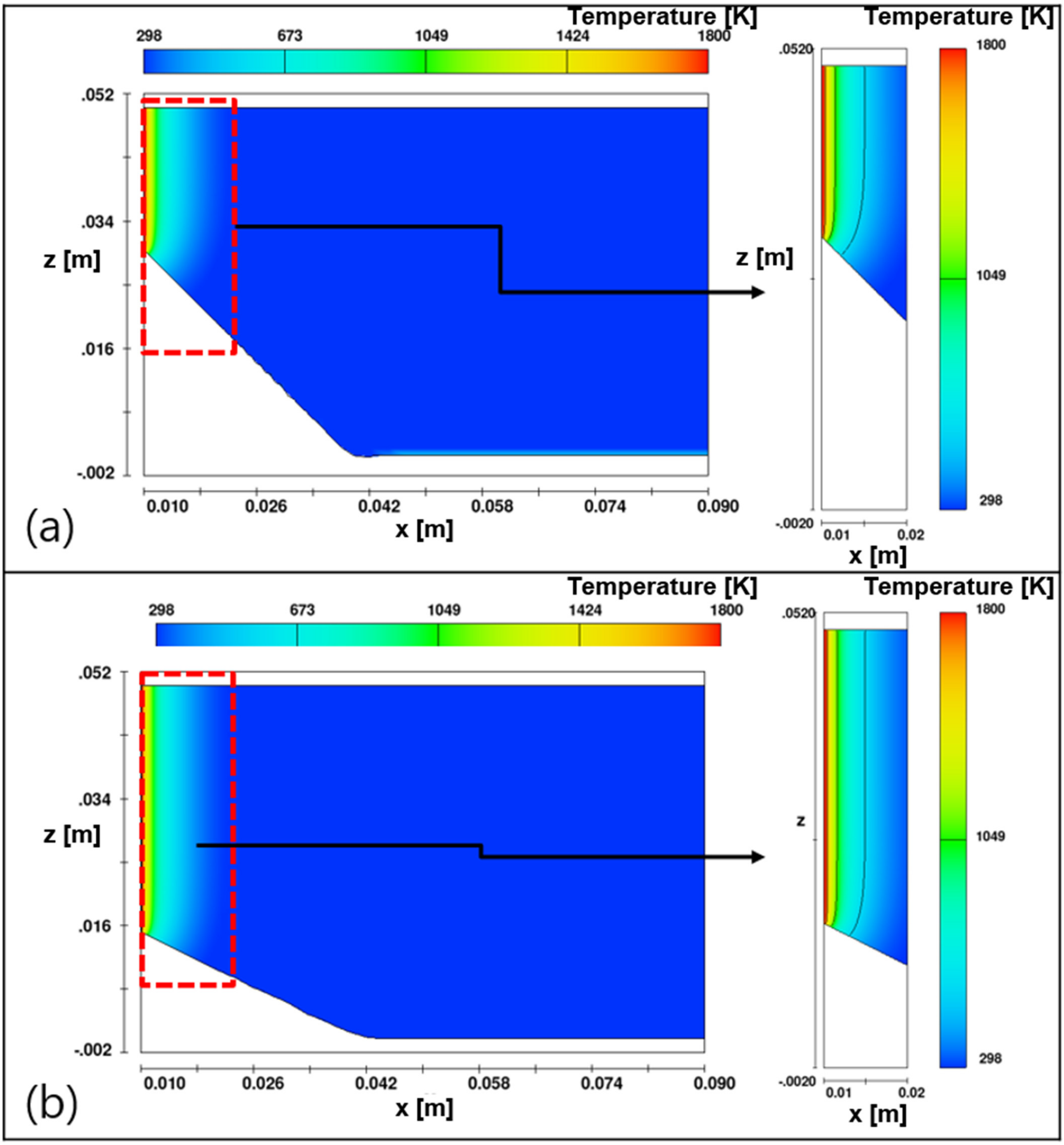

Figure 12. Laser cutting simulation result of cutting surface. (**a**) Cut surface at 10 mm in the x-direction of case 2 (**b**) Cut at 10 mm in the x-direction of case 4.

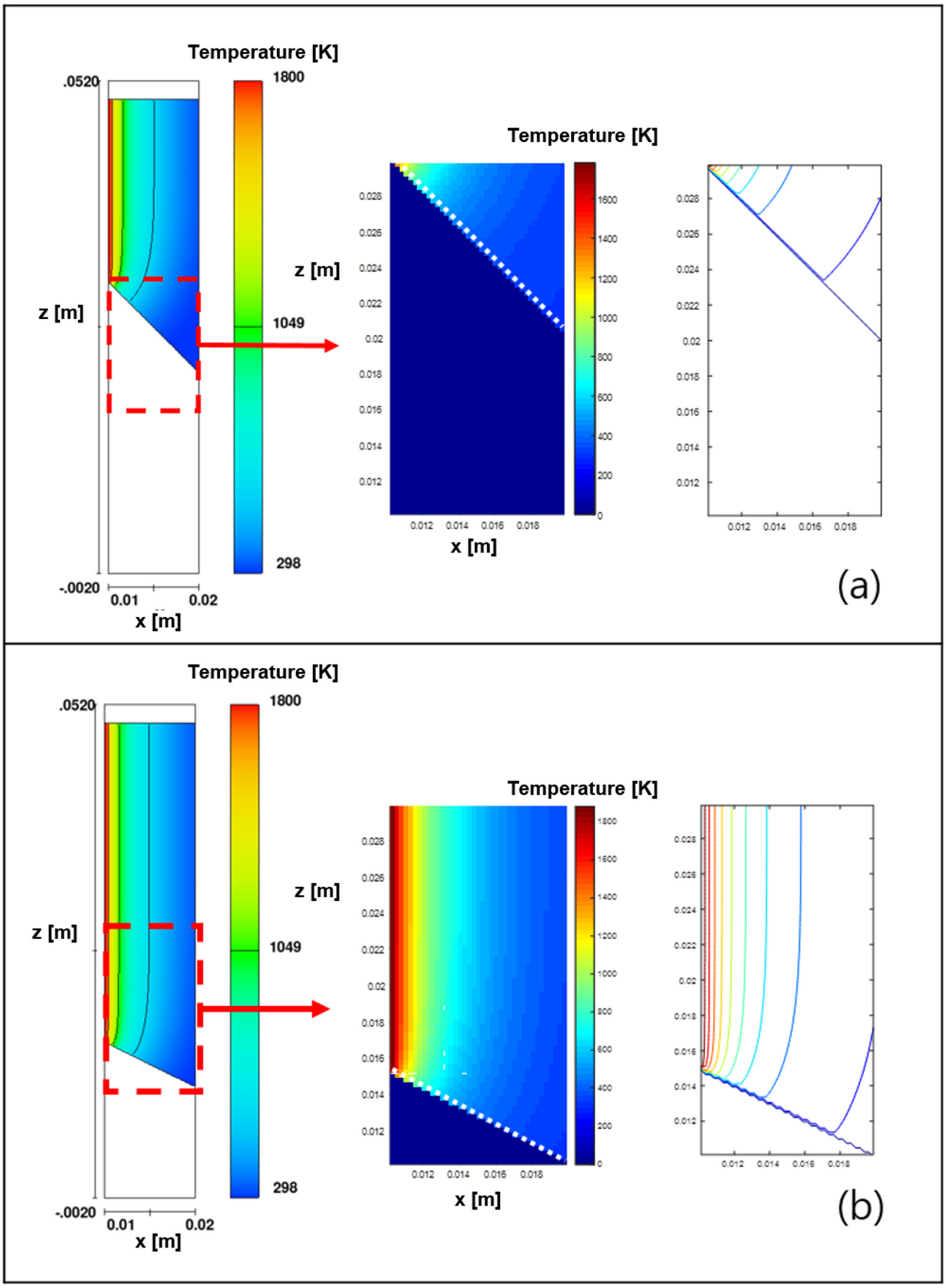

Figure 13. Laser cutting simulation results (**a**) Enlarged section of case 2 (**b**) enlarged section of case 4.

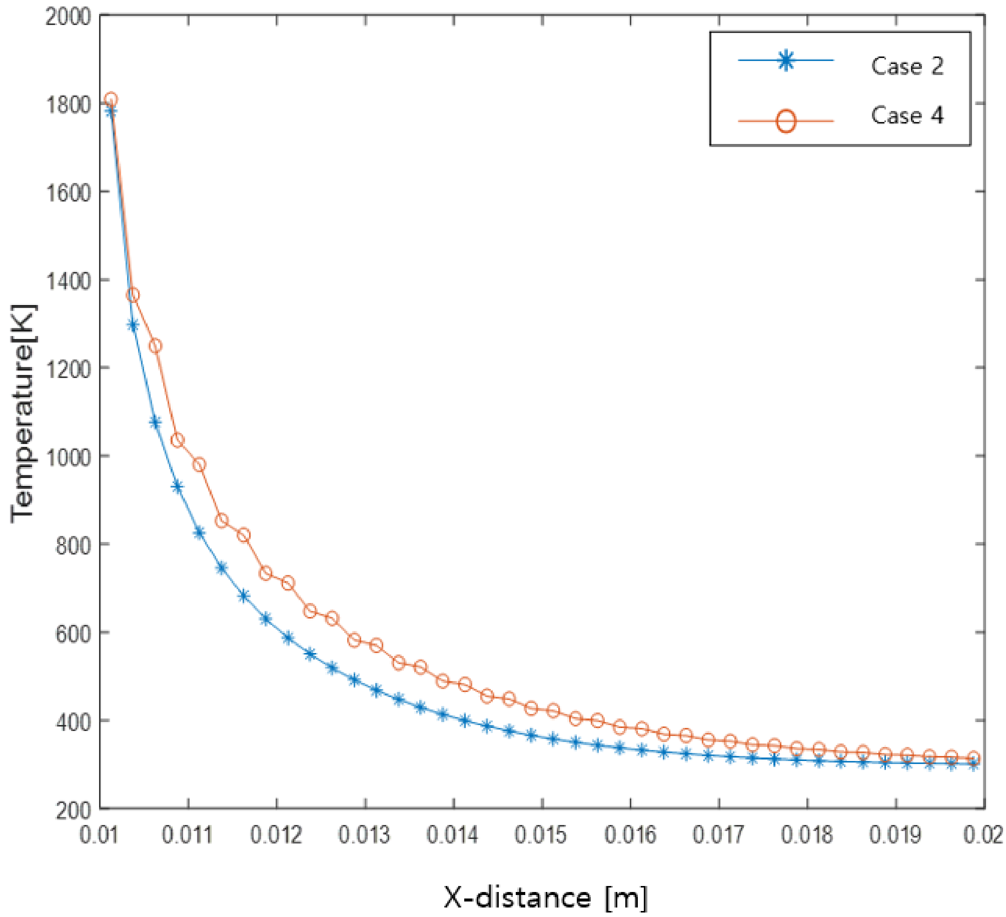

Figure 14. Comparison of simulation temperature for each position along x-direction for case 2 and case 4.

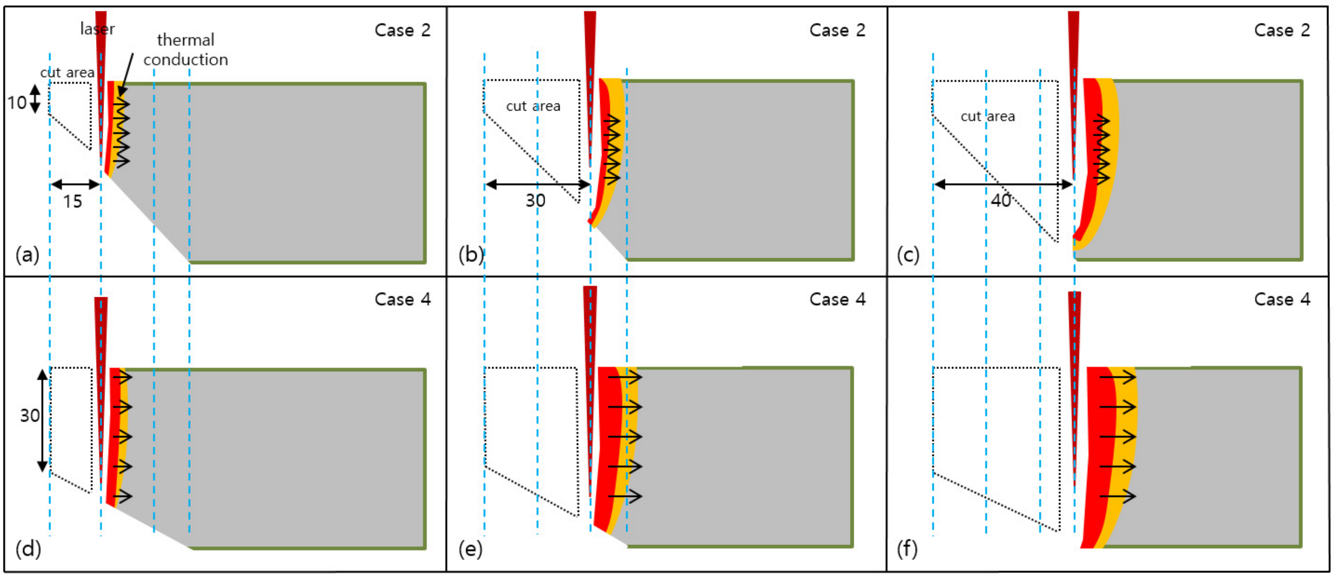

Figure 15. Visualization of thermal conduction according to the cut position of the specimen. (side-view) (**a**) case 2: 15 mm cut point, (**b**) case 2: 30 mm cut point, (**c**) case 2: 40 mm cut point, (**d**) case 4: 15 mm cut point, (**e**) case 4: 30 mm cut point, and (**f**) case 4: 40 mm cut point.

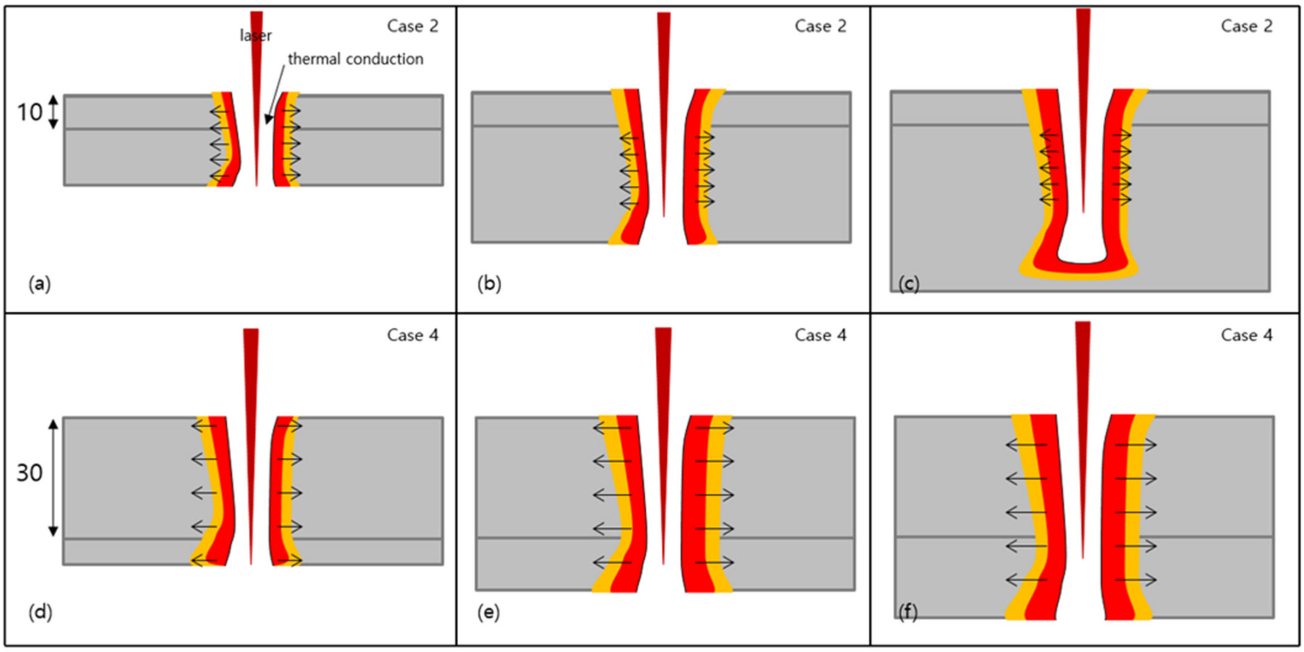

Figure 16. Visualization of thermal conduction according to the cut position of the specimen. (front side view). (**a**) case 2: 15 mm cut point, (**b**) case 2: 30 mm cut point, (**c**) case 2: 40 mm cut point, (**d**) case 4: 15 mm cut point, (**e**) case 4: 30 mm cut point, and (**f**) case 4: 40 mm cut point.

4. Conclusions

In this study, the cutting process specificity was analyzed according to different diagonal material shapes. Laser cutting was performed using an edge start method with a high-power disk laser. A STS304 specimen was used as the object, and the diagonal shape on the bottom surface was applied differently. The evacuation and spatter of the molten pool that occurred during cutting could be observed using a high-speed camera. As a result of observation with a high-speed camera, when the laser cutting is smooth, the molten metal is well evacuated to the lower surface in the vertical direction, and the difference between the location of LHP and MEP is small. On the other hand, if the cutting is not smooth, the difference between LHP and MEP increases, and eventually the molten metal is evacuated toward the upper surface of the material, and spatter is observed on the upper surface. When the cut-front temperature was the same and the initial cutting thickness is relatively thick, the area of the cutting surface is wide and the heat conduction in the cutting direction is activated. In other words, it was observed through numerical analysis that the size of preheating effect varies greatly depending on the initial thickness in the edge start cutting method. This effect can be used as a reference for the initial processing state while cutting thick metals as it is a characteristic that has not been revealed before.

Author Contributions: Conceptualization, J.C. and D.-W.C.; Methodology, R.K.; Validation, S.K. and S.-H.A.; Formal analysis, D.S.; Writing—original draft, J.C.; Writing—review & editing, D.-W.C.; Project administration, J.S.; Funding acquisition, J.S. All authors have read and agreed to the published version of the manuscript.

Funding: This research was funded by the Korea Institute of Energy Technology Evaluation and Planning All Rights Reserved, Korea (No. 20201510300350, 20201520300060) and by the National Research Foundation of Korea (No. 2019M2C9A1057806).

Institutional Review Board Statement: Not applicable.

Informed Consent Statement: Not applicable.

Data Availability Statement: Not applicable.

Conflicts of Interest: The authors declare no conflict of interest.

References

1. Lind, J.; Fetzer, F.; Blazquez-Sanchez, D.; Weidensdörfer, J.; Weber, R.; Graf, T. Geometry and absorptance of the cutting fronts during laser beam cutting. *Laser Applications.* **2020**, *32*, 032015. [CrossRef]
2. Haddadi, E.; Moradi, M.; Karimzad Ghavidel, A.; Karimzad Ghavidel, A.; Meiabadi, S. Experimental and parametric evaluation of cut quality characteristics in CO_2 laser cutting of polystyrene. *Optik* **2019**, *184*, 103–114. [CrossRef]
3. Chau, M.Q. An overview study on the laser technology and applications in the mechanical and machine manufacturing industry. *JMERD* **2019**, *42*, 16–20. [CrossRef]
4. Riveiro, A.; Quintero, F.; Lusquiñosb, F.; Val, J.; Comesaña, R.; Boutinguiza, M.; Poub, J. Experimental study on the CO_2 laser cutting of carbon fiber reinforced plastic composite. *Compos. Part A Appl. Sci. Manuf.* **2012**, *43*, 1400–1409. [CrossRef]
5. Tamura, K.; Ishigami, R.; Yamagishi, R. Laser cutting of thick steel plates and simulated steel components using a 30-kW fiber laser. *J. Nucl. Sci. Technol.* **2016**, *53*, 916–920. [CrossRef]
6. Naresh; Khatak, P. Laser cutting technique: A literature review. *Materials Today.* **2022**, *56*, 2484–2489. [CrossRef]
7. Seo, Y.; Pyo, S.; Lee, D. Experimental investigation of laser cutting on cement composites. *Welding and Joining*. **2019**, *37*, 226–230. [CrossRef]
8. Li, M.; Li, S.; Yang, X.; Zhang, Y.; Liang, Z. Fiber laser cutting of CFRP laminates with single- and multi-pass strategy: A feasibility study. *Opt. Laser Technol.* **2018**, *107*, 443–453. [CrossRef]
9. Tzanakakis, E.-G.C.; Skoulas, E.; Pepelassi, E.; Koidis, P.; Tzoutzas, I.G. The use of lasers in dental materials: A review. *Materials* **2021**, *14*, 3370. [CrossRef]
10. Zhang, Y.; Li, J.; Yang, R.; Liu, T.; Yan, Y. Analysis of kerf quality on ultrafast laser cutting of anode material for lithium-ion battery. *Opt. Lasers Eng.* **2019**, *118*, 14–21. [CrossRef]
11. Fushimi, T.; Kitazawa, M.; Endo, M.; Yamaguchi, S.; Nanri, K.; Fujioka, T. Parametric studies on improved laser cutting performance of magnesium alloy with two flow nozzles. *Jpn. J. Appl. Phys.* **2004**, *43*, 5347–5351. [CrossRef]
12. Riveiro, A.; Quintero, F.; Boutinguiza, M.; Val, J.D.; Comesaña, R.; Lusquiños, F.; Pou, J. Laser cutting: A review on the influence of assist gas. *Materials* **2019**, *12*, 157. [CrossRef]
13. Darwish, M.; Mrňa, L.; Orazi, L.; Reggiani, B. Numerical modeling and Schlieren visualization of the gas-assisted laser cutting under various operating stagnation pressures. *Int. J. Heat Mass Transf.* **2020**, *147*, 118965. [CrossRef]
14. Orazi, L.; Darwish, M.; Reggiani, B. Investigation on the inert gas-assisted laser cutting performances and quality using supersonic nozzles. *Metals* **2021**, *9*, 1257. [CrossRef]
15. Darwish, M.; Orazi, L.; Reggiani, B. Numerical analysis of the gas-assisted laser cutting flow from various supersonic nozzles. *J. Manuf. Process.* **2020**, *56*, 382–389. [CrossRef]
16. Man, H.C.; Duan, J.; Yue, T.M. Analysis of the dynamic characteristics of gas flow inside a laser cut kerf under high cut-assist gas pressure. *J. Phys. D* **1999**, *32*, 1469–1477. [CrossRef]
17. Tuladhar, U.; Ahn, S.-H.; Cho, D.-W.; Kim, D.-H.; Ahn, S.; Kim, S.; Bae, S.-H.; Park, T.-K. Analysis of gas flow dynamics in thermal cut kerf using a numerical and experimental approach for nozzle selection. *Processes* **2022**, *10*, 1951. [CrossRef]
18. Christophe, J.; Planquart, P. Diagnostics for laser cutting efficiency using computational fluid dynamics. *Procedia Manuf.* **2019**, *29*, 375–382. [CrossRef]
19. Kovalev, O.B.; Yudin, P.V.; Zaitsev, A.V. Modeling of flow separation of assist gas as applied to laser cutting of thick sheet metal. *Appl. Math. Model.* **2009**, *33*, 3730–3745. [CrossRef]
20. Madić, M.; Petrović, G.; Petković, D.; Antucheviciene, J.; Marinković, D. Application of a Robust Decision-Making Rule for Comprehensive Assessment of Laser Cutting Conditions and Performance. *Machines* **2022**, *10*, 153. [CrossRef]
21. Tuladhar, U.; Ahn, S.-H.; Cho, D.-W.; Kim, D.-H.; Ahn, S.; Kim, S.; Bae, S.-H.; Park, T.-K. Numerical modeling of an impinging jet flow inside a thermal cut kerf using CFD and schlieren method. *Appl. Sci.* **2022**, *12*, 9557. [CrossRef]
22. Cho, D.-W.; Choi, J.; Lee, S.; Shin, D. Analysis of gas flow behavior in the laser cutting process using the schlieren method and image processing. *J. Weld. Join.* **2020**, *38*, 569–575. [CrossRef]
23. Kim, D.; Cho, D.; Jo, Y.; Suh, J.; Choi, K.; Kim, R.; Ahn, S. Characteristic Analysis of Double Arcing on the Top Surface of STS304 in Plasma Arc Piercing. *J. Weld. Join.* **2021**, *39*, 427–434. [CrossRef]
24. Sim, A.; Chun, E.; Cho, D.; Chun, E.-J.; Cho, D.-W. Numerical Simulation of Surface Softening Behavior for Laser Heat Treated Cu-Bearing Medium Carbon Steel. *Met. Mater. Int.* **2020**, *26*, 1207–1217. [CrossRef]
25. Kong, F.; Santhanakrishnan, S.; Lin, D.; Kovacevic, R. Modeling of temperature field and grain growth of a dual phase steel DP980 in direct diode laser heat treatment. *J. Mater. Process. Technol.* **2009**, *209*, 5596–6003. [CrossRef]